

# Acoustic Power for Swarms of Microscopic Robots

Tad Hogg

Institute for Molecular Manufacturing  
Palo Alto, CA 94301

June 9, 2021

## Abstract

Ultrasound can power implanted medical devices. This paper evaluates its feasibility for microscopic robots in tissue that mechanically harvest energy using pistons. At these sizes, viscous drag dominates the piston motion and acoustic attenuation limits how far power can reach. Combining these factors shows that frequencies around 100kHz can deliver hundreds of picowatts to well-separated micron-size robots in low-attenuation tissues within about 10cm of the skin. However, applications of microscopic robots could involve large numbers, in which case the robots themselves significantly increase acoustic attenuation. Robots can mitigate this attenuation using cooperative swarm behaviors, with trade-offs among individual power, group performance and the complexity of the robot controllers. With such mitigating behaviors, acoustic power can be useful for swarms of a few hundred billion robots in the body, that each use tens of picowatts, on average, and can tolerate significant variability in available power, e.g., as robots in the bloodstream move from near the skin to deep within the body, or from low- to high-attenuation tissue such as the lungs.

## 1 Introduction

As implanted medical devices become smaller, more numerous and more capable, they will enable many high-precision applications [13, 52]. Of particular interest is the eventual development of micron-size robots. These are small enough to travel through even the tiniest blood vessels, but also large enough to possibly have enough computation, sensing and communication to coordinate complex activities with single-cell resolution [22, 29, 44, 51]. When used in large numbers, micron-size robots can provide precision medicine with access to individual cells [37]. Such robots are considerably smaller than micromachines [7] based on microelectromechanical systems (MEMS) which are too large to access individual cells. On the other hand, these microscopic robots are much larger than nanoparticle-based drug delivery, which can only incorporate a few logic operations [14] and so have a much more limited ability to evaluate patterns of sensed data from cells or coordinate their activities.

Among the significant challenges in realizing the benefits of swarms of microscopic robots is providing power [3, 5]. Among the options for powering small devices [9, 22], ultrasound has some appealing advantages. These include noninvasive power from transducers on the skin without requiring tethers, and the relative simplicity of mechanical energy harvesting. As an external power source, ultrasound can be easily turned on or off to control when and where robots are active. This capability is particularly useful for microscopic robots since it moves some control decisions from the robot to people or conventional controllers outside the body. This can simplify the robots by reducing the sophistication of their internal controllers.

Ultrasound can provide a variety of capabilities for implanted devices in addition to power. These include locomotion [50, 59], such as moving micron-size particles in the bloodstream [11], and cooperative interactions among neighboring devices in a swarm [50]. Moreover, ultrasound can alter the robots local environments to aid their tasks, such as selectively opening the blood-brain barrier

speed of sound	$c$	1500 m/s
density	$\rho$	$10^3 \text{ kg/m}^3$
amplitude absorption coefficient		
soft tissue	$\alpha_{\text{tissue}}$	8.3/MHz/m
lung	$\alpha_{\text{tissue}}$	470/MHz/m

Table 1: Representative acoustic properties of tissue.

for drug delivery [41, 55, 65, 68]. Ultrasound also provides high-resolution functional imaging [54], which could help guide robots to target areas in the body and identify when a sufficient number are in position to begin an activity requiring coordinated actions using sensed values from neighboring cells. Thus, while providing power, ultrasound can also help control the robots and create suitable microenvironments for them.

Ultrasound power often uses piezoelectric energy harvesters [61, 69]. Piezoelectric materials convert pressure variations to electricity. The triboelectric effect can also generate electric power for implanted devices from ultrasound [28]. An alternative, and the focus of this paper, is direct mechanical energy harvesting [12]. Mechanical harvesters avoid the need to distribute electricity within the robot, possibly with large resistive losses, and mechanisms to convert electricity to mechanical motion needed to actuate machines on the robot surface, e.g., for locomotion [46], or within the robot, e.g., mechanical computers [40, 48]. The effectiveness of mechanical harvesters is limited by their material properties, such as friction drag. To estimate the ultimate potential of ultrasound power for microscopic robots, this paper considers atomically precise materials currently under development [2, 13, 17] that could be used to build the harvesters.

The remainder of this paper first describes sound propagation in tissue, which determines how much sound energy reaches a robot inside the body. The following section evaluates how much power a single robot can extract from this sound using pistons. The paper then determines the increased attenuation due to a swarm of robots extracting energy from sound. Thus, in contrast to evaluating power for only one or a few microscopic robots, this paper quantifies how large numbers of robots affect the available power, and how these swarms can collectively mitigate those effects. Based on this analysis, the paper concludes with a discussion of the feasibility of acoustic power for swarms of microscopic robots.

## 2 Acoustics in Tissue

Sound consists of longitudinal waves propagating through materials [58, 66, 73]. This paper considers robots in tissue with representative acoustic properties given in Table 1 and the range of frequencies shown in Table 2. Even the highest frequencies have wavelengths much larger than the robot size. For these frequencies, acoustic attenuation in tissue is proportional to frequency and is conveniently quantified by the amplitude absorption coefficient  $\alpha_{\text{tissue}}$ , given in Table 1 for representative low- and high-absorption tissues [22]. Acoustic pressure of frequency  $f$  decreases by a factor of  $\exp(-\alpha_{\text{tissue}}fx)$  over a distance  $x$ . Acoustic power, which is proportional to the pressure squared, decreases twice as rapidly.

Since tissue attenuation increases rapidly with frequency, powering devices deep within the body requires frequencies below about 1 MHz. On the other hand, the frequencies should be high enough to not be audible. These considerations lead to the range frequencies given in Table 2.

Ultrasound imaging typically uses a single transducer covering a small portion of the skin. For powering devices throughout the body, multiple transducers distributed over the body ensure that each device is relatively close to a transducer. Specifically, this study evaluates power available within about 20 cm of the nearest transducer. This corresponds to using multiple transducers to cover the body, or at least the part of the body where robots require power to perform their tasks.

frequency	wavelength	$k r_{\text{robot}}$
20 kHz	75 mm	$8 \times 10^{-5}$
100 kHz	15 mm	$4 \times 10^{-4}$
1000 kHz	1.5 mm	$4 \times 10^{-3}$

Table 2: Sound frequencies and wavelengths compared to the robot size:  $k = 2\pi/\lambda$  is the wave number of sound with wavelength  $\lambda = c/f$  at frequency  $f$ , and  $r_{\text{robot}} = 1 \mu\text{m}$  is the robot’s radius.

piston		
piston diameter	$d$	300 nm
piston thickness	$\tau$	10 nm
piston range of motion	$2a$	200 nm
piston cross section area	$A = \pi(d/2)^2$	$0.071 \mu\text{m}^2$
piston sliding area	$A_{\text{sliding}}^{\text{piston}} = \pi d \tau$	$0.019 \mu\text{m}^2$
constant-force spring		
perpendicular overlap	$L_{\text{spring}}$	$\approx 35 \pm 10 \text{ nm}$
parallel overlap	$h_{\text{spring}}$	up to $\approx 200 \text{ nm}$
housing		
housing diameter	$D$	340 nm
housing depth	$H$	440 nm

Table 3: Geometry of a piston, constant-force spring and housing. Overlaps for the constant-force spring vary with piston position and ambient pressure (see Fig. 2).

### 3 Extracting Energy from Acoustic Pressure Waves

Pistons moving in response to changing pressure can extract energy from acoustic waves. Fig. 1 shows the geometry of a piston, constrained to move over a limited range within a housing. The figure does not include linkages from the piston to mechanisms within the robot powered by the piston’s motion.

Sound consists of pressure variations around an ambient value. The ambient pressure varies with time and position within the body [22]. For example, a robot moving with the blood encounters decreasing pressure of about 20 kPa over about 10 s as it moves from arteries to veins. In addition, pressure in arteries varies by about 5 kPa during each heartbeat.

A piston with a fixed restoring force would respond to acoustic pressure only when the force from the ambient pressure is close to that restoring force. Outside that range, the piston would be pinned at one of its limits of motion and not collect energy. To avoid this limitation, the restoring force must adjust to changing ambient pressure. Since ambient pressure changes much more slowly than acoustic variation, the force could be adjusted based on the average pressure on the piston measured over multiple periods of the acoustic wave. This measurement could use force sensors on the piston mechanism or pressure sensors elsewhere on the robot surface [22]. Alternatively, the controller could measure the average position of the piston and adjust the restoring force to keep the average near the middle of the piston’s range. For example, a controller could adjust the restoring force by averaging over several milliseconds to adapt to changes in ambient pressure.

The remainder of this section describes a mechanism to adjust to ambient pressure changes, the resulting piston motion, and the power extracted from acoustic pressure waves.

#### 3.1 Constant-Force Springs

One approach to compensating for ambient pressure is a conventional spring, in which restoring force is proportional to displacement. However, the increasing force with displacement stores much

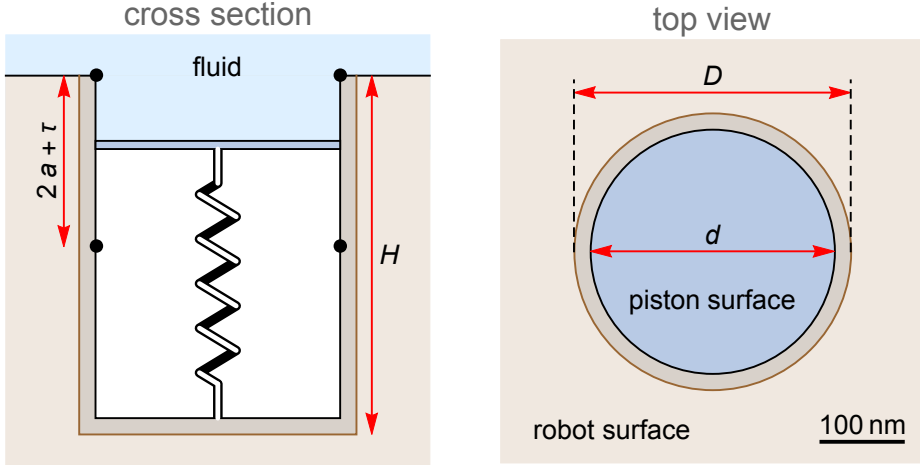


Figure 1: Cross section and top views of a piston (gray) and its housing (dark brown) in a robot. In the cross section, the large black points indicate the limits of piston motion, i.e., the upper limit for the top of the piston and the lower limit for the bottom of the piston. The distance between these points is the sum of the range of motion,  $2a$ , and the piston thickness,  $\tau$ . The spring under the piston provides a restoring force. In the top view, the scale bar corresponds to values in Table 3.

of the energy from an increasing acoustic pressure in the potential energy of the spring. Without additional mechanisms to capture that energy, the potential energy would be returned to the fluid when the pressure decreases, leading to scattering rather than absorption of acoustic energy.

Constant-force springs are a better way to adjust for ambient pressure changes. For example, a pre-compressed conventional spring with applied forces small compared to that compression has relatively small displacements around the compressed location. In this case, Hooke's Law gives nearly constant force over the range of displacements.

At the nano scale, overlapping molecular devices can behave as constant-force springs due to van der Waals interactions [10, 45]. The force is in the direction of increasing overlap. This leads to the geometry in Fig. 2, where the sheet attached to the piston is below the horizontally-adjustable sheet attached to the housing. In this configuration, the spring pushes upwards, against the pressure on the piston from the fluid. The force is proportional to the length of overlap,  $L_{\text{spring}}$ , between the sheets in the direction perpendicular to the motion:

$$F_{\text{spring}} = K_{\text{spring}} L_{\text{spring}} \quad (1)$$

Unlike Hooke's law, this force is independent of the position in the direction of motion,  $h_{\text{spring}}$ . The spring constant  $K_{\text{spring}}$  is 0.16 N/m for nested nanotubes [10] and 0.2 N/m for graphene sheets [45]. Sheets are convenient for this application because a horizontal change in their position, i.e., changing  $L_{\text{spring}}$ , allows adjusting the spring's force in response to changing ambient pressure.

For example, the force on a piston with area given in Table 3 due to one atmosphere of external pressure is 7 nN. The constant-force spring compensates for this force with an overlap  $L_{\text{spring}} = 35$  nm. This overlap is considerably less than the piston diameter, allowing more than enough room for the overlapping sheets within the piston housing.

In the geometry of Fig. 2, the vertical extent of each sheet must be at least equal to the range of piston motion. This limits the piston's range to less than a third of the housing depth. More efficient use of housing volume is possible because horizontal overlaps several times larger than 35 nm can fit within the housing diameter. Thus the constant-force spring could connect to the piston via a lever: a larger overlap would increase the spring's force enough to compensate for pressure on the piston while the vertical overlap of the sheets changes by a corresponding multiple smaller than the

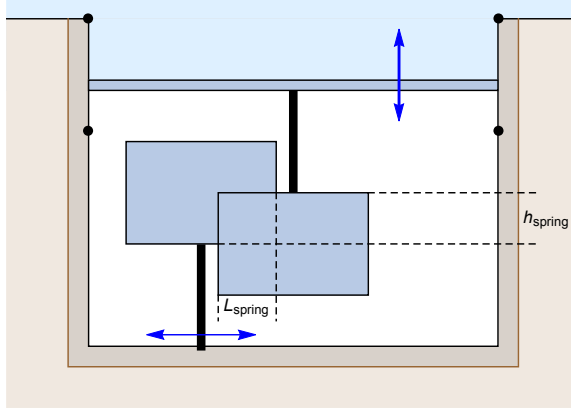


Figure 2: Overlapping sheets forming an adjustable constant-force spring. The thick vertical lines connect the sheets to the piston or housing. These connections could be offset from the plane of overlap between the sheets to avoid limiting the sheets' motions. The lower sheet moves vertically with the piston (indicated by the vertical arrow), thereby changing the vertical overlap,  $h_{\text{spring}}$ , between the sheets. Moving the position of the upper sheet's attachment to the housing (indicated by the horizontal arrow) adjusts the horizontal overlap,  $L_{\text{spring}}$ . Horizontal scale is exaggerated compared to Fig. 1.

piston's movement. Thus the sheets could have smaller vertical extent, and the piston could move through a greater fraction of the housing, than in Fig. 2. This would allow a greater range of piston motion in a given housing depth, or reducing the housing depth required for a given range of motion, thereby reducing the housing volume and providing more space in the robot for other devices.

The constant-force spring in Fig. 2 consists of two sheets sliding over each other. These sheets could be much thinner than the piston diameter, so the housing could contain multiple sliding sheets with separate actuators to adjust their overlaps independently. This would provide redundancy against failures, or allow different motors to handle adjustments over different ranges of forces. Alternatively, the force could come from combining one or more adjustable planes with nested nanotubes, whose forces are not adjustable. In this case, the nanotubes could provide the force for the lowest ambient pressure in the body, while the adjustable planes provide forces over the range of ambient pressure above this minimum value.

### 3.2 Piston Friction

At the small sizes considered here, frictional drag is the dominant force on robot mechanisms. Thus, assessing the feasibility of mechanical energy harvesting must account for friction, which depends on surface size and structure [36]. Specifically, drag force on a piston moving at speed  $v$  is

$$F_{\text{drag}} = k_{\text{total}}v \quad (2)$$

with the drag coefficient

$$k_{\text{total}} = k_{\text{f}} + k_{\text{load}} \quad (3)$$

having contributions from internal friction of piston motion,  $k_{\text{f}}$ , and from powering mechanisms within the robot,  $k_{\text{load}}$ . Contributions to  $k_{\text{load}}$  include, for instance, friction within robot components such as mechanical computers [48], driven by a piston's motion.

Internal friction consists of viscous drag from motion through the fluid around the robot,  $k_{\text{viscous}}$ , and sliding friction between the piston and its housing, which, for atomically smooth surfaces, has the form  $k_{\text{sliding}}A_{\text{sliding}}$  [16], where  $k_{\text{sliding}}$  is the sliding drag coefficient and  $A_{\text{sliding}}$  is the area of the sliding surfaces. Thus

$$k_{\text{f}} = k_{\text{viscous}} + k_{\text{sliding}}A_{\text{sliding}} \quad (4)$$

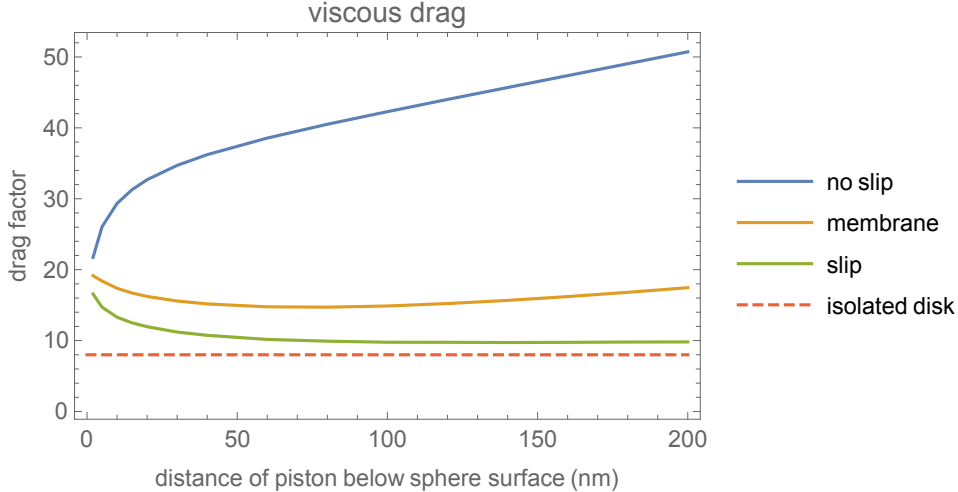


Figure 3: Viscous drag factor,  $g = k_{\text{viscous}}/(d\eta)$ , for the piston described in Table 3 as a function of its position below the robot surface for the boundary conditions described in the text. The dashed line is the value for an isolated disk moving face-on through the fluid.

Friction arising from motion of linkages connecting the piston to devices within the robot are considered part of dissipation external to the piston included in  $k_{\text{load}}$ . The remainder of this section estimates the magnitude of these contributions to  $k_f$ .

### 3.2.1 Viscous Drag

The first contribution to  $k_f$  in Eq. (4) arises from viscous drag in the fluid. An object moving at speed  $v$  through a fluid with viscosity  $\eta$  at low Reynolds number experiences a drag force proportional to its size and the fluid viscosity [26]. A convenient characterization of this drag is the viscous drag factor  $g = k_{\text{viscous}}/(d\eta)$ , where  $d$  is the object's size. The value of  $g$  depends on the object's shape and orientation, as well as any nearby boundaries. For instance, in unbounded fluid, a sphere with diameter  $d$  has  $F_{\text{drag}} = 3\pi\eta dv$  [6], so  $g = 3\pi$ . Similarly, a flat disk with diameter  $d$  moving face-on through the fluid has  $g = 8$  [6].

Numerically evaluating the fluid flow gives the viscous drag as a function of the piston's position within its housing. The drag depends on how the fluid interacts with the housing surface; in particular, the deviation from the no-slip boundary condition between fluids and solid surfaces [47, 63]. The fluid motion considered here has large velocity gradients near the edge of the moving piston, which can lead to some slip [24, 43]. While direct experimental measurements of the slip are difficult, molecular dynamics simulations identify factors affecting slip [4], though such computations are generally restricted to short distances and time scales and use shear rates considerably larger than the flows considered here. Factors affecting the boundary condition include the structure of the fluid on nanometer length scales and its composition, particularly the amount of dissolved gases. A precise estimate of the boundary conditions and hence the piston drag will require experimental investigation.

Due to this range of possibilities, this study evaluates the drag with several boundary conditions on the fluid's motion at the housing wall: 1) no-slip except for slip within 1 nm of the piston's surface due to the high shear between the stationary housing and moving piston, 2) an elastic membrane between housing and piston so that fluid speed changes linearly between them, and 3) slip along the housing wall, e.g., due to suitably engineered surface or an approximation to the reduced slip at high shear from dissolved gases. Fig. 3 shows the drag factor  $g$  for a piston with parameters given in Table 3 with these choices. For comparison, the dashed line shows the drag on an isolated disk moving face-on through the fluid far from any boundaries.

Based on Fig. 3, this study uses a relatively large value,  $g = 45$ , and, for simplicity, takes the value to be independent of piston position. This gives  $k_{\text{viscous}} = gd\eta = 1.4 \times 10^{-8} \text{ kg/s}$  for the value of  $\eta$  given in Table 5. In practice, the housing surface may allow more slip at the boundary, so this choice approximates a lower bound on acoustic power.

### 3.2.2 Sliding Drag

The second contribution to  $k_f$  in Eq. (4) is friction from sliding surfaces. For stiff materials, theoretical estimates for atomically-flat surfaces give  $k_{\text{sliding}}$  as somewhat less than  $10^3 \text{ kg}/(\text{m}^2\text{s})$  [16, 22] for speeds well below the speed of sound, as is the case for piston motion. Thus  $k_{\text{sliding}} = 10^3 \text{ kg}/(\text{m}^2\text{s})$  is used here to estimate an upper bound for sliding friction.

The sliding area includes the surface at the edge of the piston next to the housing and the overlapping surface of the constant-force spring:

$$A_{\text{sliding}} = A_{\text{sliding}}^{\text{piston}} + L_{\text{spring}}h_{\text{spring}} \quad (5)$$

The overlap area of the constant-force spring,  $L_{\text{spring}}h_{\text{spring}}$  is less than  $0.01 \mu\text{m}^2$ , so Table 3 gives  $A_{\text{sliding}} < 0.03 \mu\text{m}^2$ . Thus  $k_{\text{sliding}}A_{\text{sliding}} < 3 \times 10^{-11} \text{ kg/s}$  is much less than the viscous drag estimate in Section 3.2.1, i.e.,  $k_f \approx k_{\text{viscous}}$ .

The above discussion estimates the drag on the piston as it moves in response to acoustic pressure variation. In addition, actuators alter the overlap  $L_{\text{spring}}$  of the constant-force spring in response to changes in ambient pressure. The sliding drag during this adjustment is

$$F_{\text{drag}}^{\text{spring}} = k_{\text{sliding}}(L_{\text{spring}}h_{\text{spring}}) \frac{dL_{\text{spring}}}{dt} \quad (6)$$

An example is the changing ambient pressure during a heartbeat of about  $p = 5 \text{ kPa}$  in one second. This requires changing  $L_{\text{spring}}$  by 2 nm. Using the bound on sliding area described above, i.e,  $L_{\text{spring}}h_{\text{spring}} < 0.01 \mu\text{m}^2$ , the dissipation due to friction during this change is negligibly small, less than  $10^{-16} \text{ pW}$ . The small size of this value is due to the relatively long time over which ambient pressure changes, and the consequent slow speed required to adjust the overlap of the constant-force spring.

Actuators adjusting the horizontal position of the surfaces apply forces comparable to  $F = K_{\text{spring}}h_{\text{spring}}$  to change the overlap  $L_{\text{spring}}$ . To reduce overlap by  $\Delta L_{\text{spring}}$ , the actuator does work  $W = F\Delta L_{\text{spring}}$ . The overlap  $h_{\text{spring}}$  varies with the piston's position. A typical example for the geometry of Fig. 2 is  $h_{\text{spring}} = 100 \text{ nm}$  and  $F = 20 \text{ nN}$ . Theoretical estimates indicate that, for example, electrostatic actuators [16] could provide such forces and be small enough to adjust overlaps for the piston sizes considered here. Continuing with the previous example of 5 kPa pressure change in one second,  $\Delta L_{\text{spring}} = 2 \text{ nm}$  so  $W = 4 \times 10^{-17} \text{ J}$ . The work done by the actuator is stored as potential energy in the position of the sheets. This energy could be recovered as work done by the sheets to increase  $L_{\text{spring}}$  when ambient pressure later increases. However, even if this work were entirely dissipated during the one second change in ambient pressure, it amounts to a still negligible dissipation of  $10^{-5} \text{ pW}$ . This potentially avoidable dissipation is much larger than that due to sliding friction described in Eq. (6), a property also seen in rotary motion of atomically precise mechanisms [34].

### 3.3 Piston Motion

For the position of the piston,  $x$ , define  $x = 0$  to be the middle of the piston's range, and pick the sign of  $x$  so positive values mean the piston is farther from the center of the robot. Let  $a > 0$  be the maximum value of  $x$ , so the piston ranges between  $-a$  and  $a$ .

The piston moves in response to forces from the applied pressure, the spring,  $F_{\text{spring}}$ , and damping,  $F_{\text{drag}}$ . The pressure is  $p_{\text{ambient}} + p(t)$  where  $p(t)$  is the acoustic pressure, and  $p_{\text{ambient}}$  is the ambient fluid pressure. Fluid pressure pushes inward and the spring pushes outward. The piston

stops whenever these forces attempt to push it beyond its range of motion. Thus, unless the piston is stopped at a limit to its range of motion, its position  $x$  changes according to

$$m \frac{d^2x}{dt^2} = -F_{\text{drag}} + F_{\text{spring}} - (p_{\text{ambient}} + p(t)) A \quad (7)$$

where  $A$  is the cross section area of the piston and  $m$  its mass.

Viscous forces dominate the motion of objects of the size and speeds considered here [56]. This means that the piston moves at the speed at which  $F_{\text{drag}}$  balances the forces applied to the piston. That is, the piston moves at its terminal velocity in the fluid, so Eq. (7) becomes

$$k_{\text{total}} \frac{dx}{dt} = F_{\text{spring}} - (p_{\text{ambient}} + p(t)) A \quad (8)$$

by using Eq. (2). If the piston reaches a limit to its motion, at  $x = \pm a$ , it remains there, i.e.,  $dx/dt = 0$ , until the applied force changes sign.

The constant-force spring adjusts to the ambient pressure, i.e.,  $F_{\text{spring}} = p_{\text{ambient}} A$ . We arbitrarily pick the origin of time at the minimum acoustic pressure, so  $p(t) = -p \cos(\omega t)$  for sound with angular frequency  $\omega = 2\pi f$  and amplitude  $p > 0$  at the robot's location. With these definitions, convenient dimensionless parameters for the piston motion are

$$\begin{aligned} \lambda &\equiv \frac{pA}{a\omega k_f} \\ k_{\text{ratio}} &\equiv \frac{k_{\text{load}}}{k_f} \end{aligned} \quad (9)$$

$\lambda$  is a ratio of acoustic pressure and internal drag forces on the piston. Defining normalized position  $X = x/a$  and time  $\tau = \omega t$ , Eq. (8) becomes

$$\frac{dX}{d\tau} = \frac{\lambda}{1 + k_{\text{ratio}}} \cos(\tau) \quad (10)$$

Viscous drag on the piston depends on its position (see Fig. 3). For simplicity, we ignore this variation and instead consider the drag coefficient  $k_{\text{viscous}}$ , and hence  $k_f$ , to be independent of position, as described in Section 3.2.1. In this case, Eq. (10) gives

$$X(\tau) = \frac{\lambda}{1 + k_{\text{ratio}}} \sin(\tau) \quad (11)$$

when the piston starts at the center of its range of motion, i.e.,  $X(0) = 0$ .

Eq. (11) describes the complete piston motion when  $\lambda \leq 1 + k_{\text{ratio}}$ . Otherwise, the piston spends part of each cycle stopped at the limits of its range, and Eq. (10) only holds between these stops. Fig. 4 illustrates these cases.

### 3.4 Power

As the piston moves, it dissipates energy against the drag force at the rate  $F_{\text{drag}}\dot{x} = k_{\text{total}}\dot{x}^2$ , from Eq. (2). Of this amount,  $k_{\text{load}}\dot{x}^2$  is dissipated by the load as power available to the robot.

When Eq. (11) describes the complete motion of the piston, the time-average power over a cycle of the acoustic pressure variation is

$$\begin{aligned} P_{\text{total}} &= \frac{1}{2} A^2 p^2 \frac{1}{k_{\text{total}}} \\ P_{\text{load}} &= P_{\text{total}} \frac{k_{\text{load}}}{k_{\text{total}}} \end{aligned} \quad (12)$$

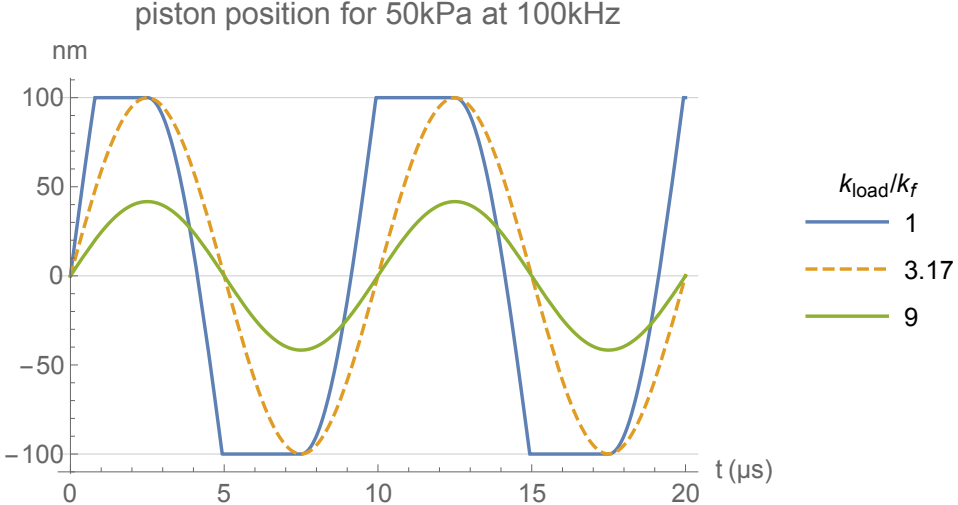


Figure 4: Motion of pistons described in Table 3 in response to acoustic pressure of 50 kPa at 100 kHz. In this case,  $\lambda = 4.17$ . The curves show the piston's position as a function of time with the piston connected to one of three loads:  $k_{\text{load}}$  equal to  $k_f$ ,  $(\lambda - 1)k_f$  (dashed) or  $9k_f$ . The dashed curve is the smallest load for which Eq. (11) describes the complete motion.

From Eq. (3), the maximum  $P_{\text{load}}$  occurs when  $k_{\text{load}} = k_f$  (i.e.,  $k_{\text{ratio}} = 1$ ) in which case  $P_{\text{load}} = P_{\text{total}}/2 = A^2 p^2/(8k_f)$ . This holds provided Eq. (11) describes the complete motion, i.e., when  $\lambda \leq 2$ .

When  $k_{\text{load}}=k_f$  and  $\lambda > 2$ , the piston stops at its limit of motion for a portion of each acoustic period. The piston delivers no power while stopped. In this case, the piston delivers more power to the load for somewhat larger values of  $k_{\text{load}}$ . In particular,  $k_{\text{ratio}} = \lambda - 1$  is the smallest load for which Eq. (11) describes the complete motion. From Eq. (12), this choice gives larger  $P_{\text{load}}$  than any larger value of  $k_{\text{load}}$ . Numerically evaluating the motion for  $k_{\text{ratio}}$  between one and  $\lambda - 1$  shows the maximum  $P_{\text{load}}$  occurs at  $k_{\text{load}}$  slightly smaller than  $\lambda - 1$ . I.e., the larger power from faster piston speed while it moves more than compensates for the lack of power during the short times the piston stops at its limit. However, this maximum is only slightly larger than  $P_{\text{load}}$  when  $k_{\text{ratio}} = \lambda - 1$ : less than 3% more for  $\lambda < 5$ , the range relevant for this discussion. Due to the minor benefit of smaller  $k_{\text{load}}$ , for simplicity we use  $k_{\text{ratio}} = \lambda - 1$  to estimate the available power when  $\lambda > 2$ .

Combining these cases gives

$$P_{\text{load}} = \begin{cases} \frac{1}{8k_f} A^2 p^2 & \text{if } \lambda \leq 2 \\ \frac{1}{2} a\omega (Ap - a\omega k_f) & \text{if } \lambda > 2 \end{cases} \quad (13)$$

At sufficiently high frequencies or low pressures,  $\lambda \leq 2$  so available power is proportional to the square of the pressure and independent of frequency. Conversely, at very low frequencies or high pressures (more specifically,  $\lambda \gg 1$ ),  $P_{\text{load}} \approx a\omega Ap/2$ , which is also  $(\pi/2)pVf$  where  $V = 2aA$  is the full displacement volume of the piston. In this limit, power used by the load is proportional to frequency and pressure, and is much larger than the power dissipated by viscous drag.

### 3.5 Piston Reliability

In response to 100 kHz sound, a piston oscillates  $10^5$  times a second. Thus a piston oscillates about a billion times during a mission lasting several hours. An important question is the reliability of pistons and their associated mechanisms for this many operations.

As an example of reliability, micromechanical machines such as MEMS mirrors readily achieve over  $10^{12}$  operations [15]. For nanoscale machines, theoretical analysis suggests atomically precise

components have low failure rates [16]. This could apply to the moving components inside the piston housing, including constant-force springs and couplings to internal robot mechanisms, because those mechanisms are protected from the external biological environment. Moreover, experimental studies of sliding in nested nanotubes show no wear at the atomic scale [10]. Thus we can expect reliable performance for mechanical devices inside the housing.

Another reliability issue is fouling of surfaces exposed to fluids. Such fouling could increase drag on the pistons, reducing the available power. Experience with implanted micro devices shows that suitable surface design can provide biocompatibility and reduce fouling [25], suggesting fouling need not be a problem for operating times well beyond a few hours.

However, if fouling is a significant problem over the duration of a mission, modifications to the devices could reduce the problem. For instance, the piston could be covered with a watertight membrane connected to the upper edge of the housing. This would exclude external fluids from the housing, thereby avoiding fouling along the housing sides. This approach would somewhat reduce available power because some energy would be dissipated in stretching the membrane. An alternative approach is to keep some pistons covered and inactive. These pistons would act as a reserve, to be uncovered as needed to replace pistons that become stuck. The covered pistons would not collect energy, thereby reducing available power. In terms of power generation, covering some pistons would be equivalent to using all pistons with a reduced duty cycle.

One other reliability issue arises from the barriers limiting piston motion. These barriers could extend inward from the housing at the indicated locations in Fig. 1. The barrier above the piston would be in the fluid and may become fouled or alter the flow along the side of the housing to increase viscous drag. To avoid these potential problems, the barriers could be entirely inside the housing, e.g., limiting the motion of the spring mechanism rather than directly acting on the piston. With a constant-force spring consisting of atomically-precise structures, these barriers could also be atomically precise to provide well-defined performance without wear. However, if such barriers are atomically flat, they could stick to the part of the constant-force spring reaching the barrier due to van der Waals forces. Specifically, van der Waals force per unit area on planar surfaces separated by distance  $\delta$  is  $p_{\text{vdW}} = H_{\text{vdW}}/(6\pi\delta^3)$  [16, 70], with the Hamaker constant,  $H_{\text{vdW}}$ , in the range  $10^{-20}\text{--}10^{-19}\text{ J}$  [43, 70].

As an estimate of this force, suppose the barriers consist of a set of tabs extending inward from the housing, with total area of  $10\text{ nm}^2$  coming into contact with part of the spring or piston to stop its motion. If these were atomically smooth surfaces, contact with atomic spacing of about  $0.3\text{ nm}$  results in van der Waals force of about  $2\text{ nN}$ , using the upper range of values for  $H_{\text{vdW}}$ . This force is comparable to the force on the piston due to variation in acoustic pressure near the transducers (see Section 3.1). Thus van der Waals forces could keep the piston stuck at its limit even when the acoustic pressure changes sign and acts to push it away from the limit. This would be particularly problematic when acoustic pressure variation is small, i.e., for robots deep within the body or in high-attenuation tissue. However, when the pressure variation is small, the piston will not reach the limits of its motion, as discussed in Section 3.3, thereby avoiding the problem. If necessary, adding extrusions on the surfaces so only a small portion of the surfaces come into contact [16, 23] can avoid this difficulty.

## 4 Acoustic Power for a Robot

Safety limits ultrasound intensity to about  $1000\text{ W/m}^2$  for extended use [53, 60], which corresponds to pressure amplitude  $p = 55\text{ kPa}$  because the time-average energy flux of a plane wave is

$$\mathcal{F} = \frac{1}{2} \frac{p^2}{\rho c} \quad (14)$$

where  $p$  is the amplitude of sound pressure variation,  $\rho$  is the fluid density and  $c$  the speed of sound. For transducers well-coupled to the skin over soft tissues, reflection losses can be fairly low, e.g., 10%. Other cases have larger losses, e.g., 40% for transit through the skull [22].

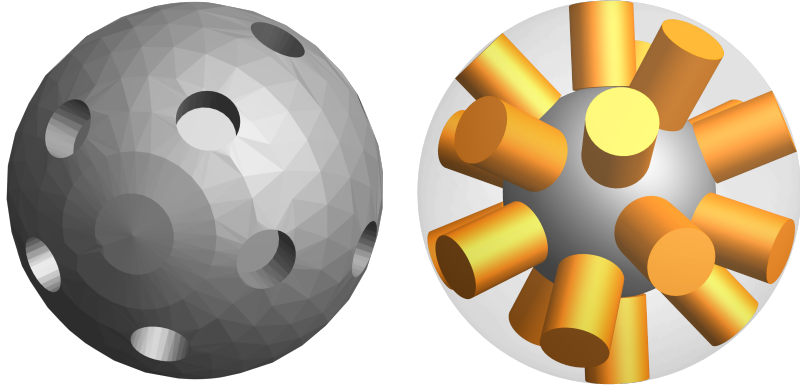


Figure 5: A robot with twenty pistons. Left: robot with fully retracted pistons. Right: robot with transparent surface to show the pistons and their housings within the robot. The inner sphere indicates the portion of the robot volume under the pistons and their housings. Table 3 gives the geometry of each piston.

pistons	
duty cycle	50%
number	20
fraction of robot volume	19%
fraction of robot surface	14%

ultrasound source	
intensity	1000 W/m <sup>2</sup>
reflection loss	10%
source pressure	50 kPa

Table 4: Robot power scenario for the example shown in Fig. 5. The fractions include the piston’s housing, indicating how much of the robot these devices use. Inside the robot, the bottoms of the pistons use 46% of the surface area indicated by the inner, solid sphere of the figure. The pistons themselves, i.e., the moving portion of the device, use  $f_{\text{surface}} = 11\%$  of the robot’s surface area. The sound source intensity corresponds to 55 kPa (see Eq. (14)), which is reduced by the reflection loss to give the source pressure in the tissue next to the transducer.

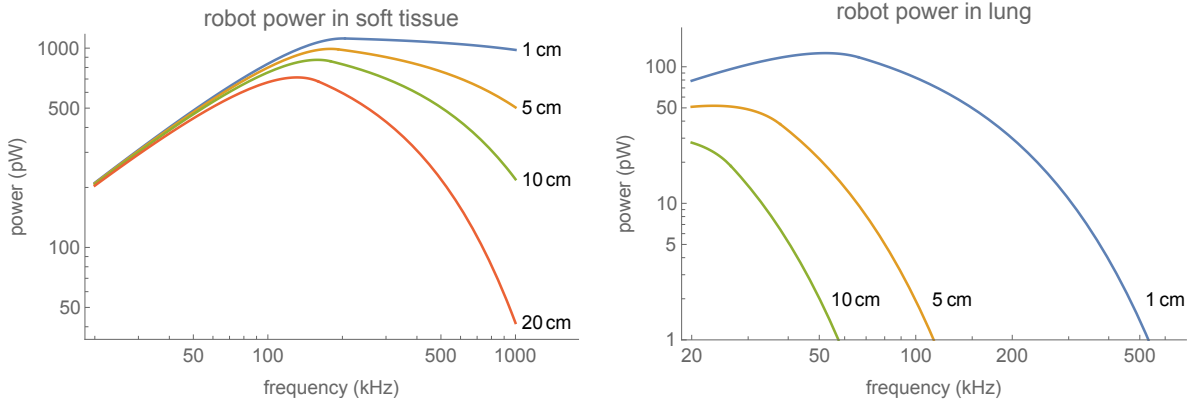


Figure 6: Power for a robot at various distances from the ultrasound transmitter in soft tissue and lung, for the scenario of Table 4. The value next to each curve indicates distance from the skin or from the skin-facing surface of the lung, for soft tissue and lung, respectively.

A robot can use multiple pistons to extract power, as illustrated in Fig. 5. An example is the scenario in Table 4. The operating duty cycle could arise from variation in sound pressure at the robot’s location due to adjustments to the transducer to shift the location of minimum pressure variation in standing waves. For example, these changes could shift the sound field by half a wavelength to ensure robots are not permanently located in a pressure minimum due to interference from strong reflections, e.g., from nearby bones. The duty cycle could also arise from a robot occasionally turning off power collection to enable (or simplify the design or control of) other uses for its surface that are affected by piston motions. Examples include using surface vibrations for communication [33] or locomotion [30]. Another reason to occasionally turn off the pistons arises from their motion altering the fluid flow near the surface, and thus the pattern of fluid stresses on the robot surface. Such changes could degrade the accuracy of a robot using these stresses to estimate its position and motion [31]. Turning off the pistons when performing these estimates avoids this problem. Alternatively, if there is no need for pistons to operate with a duty cycle, the results given here correspond to a robot with 10 pistons operating continually, i.e., 100% duty cycle, thereby leaving more surface area for other uses, e.g., chemical sensing.

Two robot placements illustrate the available power: in soft tissue and in a lung, which has large acoustic attenuation (see Table 1). The lung surface is about 5 cm beneath the skin, leading to some attenuation between the transducer on the skin and the surface of the lung. Furthermore, the different acoustic impedances of lung and soft tissue means only about 36% of the acoustic energy reaching the lung is transmitted into it [22]. Additional attenuation arises from the ribs, which partly cover the lungs. Bone transmits only part of the sound reaching it, and the sound that travels through bone attenuates about 20 times more rapidly than attenuation in soft tissue [22]. The power reaching various parts of the lung depends on their locations relative to the ribs and transducers on the skin [67]. An approximate accounting for these factors estimates acoustic energy for the lung as first attenuating through 5 cm of soft tissue, after which 20% of the incident energy enters the lung.

With these estimates, Fig. 6 shows power available to a robot at various distances from the skin for a typical low-attenuation case (soft tissue) and for robots in the lung. The figure indicates that frequencies around 100 kHz are best for powering robots in regions with low attenuation between the robot and the sound source. Lower frequencies, e.g., 40 kHz, are better for robots within the lung, but robots deep in the lung have much less power.

These results indicate how robot design modifications could provide more power. For instance, a robot could have more pistons, though that will reduce the volume and surface area available for other components. Somewhat larger robots could accommodate more or larger pistons. This could be useful for robots implanted at a fixed location. Increasing robot size is not suitable for robots intended to move through circulatory system: such robots cannot be much larger than the 2-micron

diameter considered here [22].

## 5 Sound Attenuation by Robots

Robots absorbing power decrease the intensity of the acoustic wave. Section 4 described how much power a robot absorbs with each piston, i.e.,  $P_{\text{total}}$ , of Eq. (12), both to overcome friction and provide power to other devices in the robot. In addition, microscopic robots are likely to be stiffer than biological tissues [22]. This gives the robots significantly different acoustic properties than tissue, which lead to scattering and dissipation in boundary layers around each robot. This section evaluates these losses, which occur whether or not a robot absorbs power.

### 5.1 Uniform Surface Response to Acoustic Pressure

The sound wavelengths considered here are much larger than the robot size (see Table 2). This simplifies the evaluation of scattering and dissipation around the robot. In particular, the long wavelength means the sound is insensitive to the distribution of features on the robot surface. Moreover, the acoustic pressure at a given time is nearly the same over the entire robot. So all pistons move in phase with each other. Thus, instead of modeling each piston individually, we can estimate a robot’s effect on the sound by treating the piston motion induced by acoustic pressure variation as its average value spread uniformly over the robot’s surface.

Specifically, Eq. (8) gives each piston’s motion in response to acoustic pressure  $p(t)$ . The constant-force spring cancels the ambient pressure, so  $dx/dt = -p(t)A/k_{\text{total}}$ . Due to the robot’s stiffness, the rest of the surface has negligible motion in response to the pressure. With pistons covering a fraction  $f_{\text{surface}}$  of the surface, the corresponding uniform response is the average of these two cases, i.e., treating the entire surface as having radial velocity  $-\beta p(t)$  where  $\beta = f_{\text{surface}}A/k_{\text{total}}$ . For the robot described in Table 4,  $f_{\text{surface}} = 11\%$ . With the parameters of Table 3, the full range of piston motion corresponds to about 2% change in sphere radius from this average motion. This leads to approximating the robot as a slightly vibrating sphere with radius  $r_{\text{robot}}$ .

This approximation of uniform surface motion and a plane wave impinging on the sphere gives an axisymmetric sound field. This sound produces elastic waves within the sphere. However, such waves have a minor effect for the long wavelengths considered here [18], which allows neglecting elastic waves and instead using a specified boundary condition on the sphere’s surface. Thus the sound around a sphere in response to an incident plane wave is approximately that arising from the boundary condition that the radial velocity of the sphere’s surface is the sum of  $-\beta p(t)$  and the radial component of the fluid velocity induced by the plane wave. For long wavelengths, the scattered sound is much weaker than the incident wave [27]. This allows replacing  $p(t)$  in the boundary condition by the pressure of the incident plane wave. With this simplification, the boundary condition does not depend on the scattered pressure, and evaluating the scattered sound follows the same procedure as for scattering from rigid objects and gas bubbles [19, 27, 64], but with the boundary conditions for a moveable surface described here.

A useful measure of an object’s effect on waves is its cross section: the ratio of scattered or absorbed power, over a cycle of the wave, to the time-average flux of the incident acoustic wave, given by Eq. (14). This area can differ substantially from the geometric surface or cross section areas of the object.

### 5.2 Scattering

For the simplified situation described in Section 5.1, the scattering cross section in the long-wavelength limit considered here (see Table 2) is [19, 64]

$$\sigma = \pi r_{\text{robot}}^2 \left( 4(k r_{\text{robot}})^2 (\beta c \rho)^2 + \frac{4}{9} (k r_{\text{robot}})^4 (1 - 12(\beta c \rho)^2) \right) \quad (15)$$

dynamic viscosity	$\eta$	$10^{-3}$ Pa s
bulk viscosity	$\eta_{\text{bulk}}$	$3 \times 10^{-3}$ Pa s
temperature	$T_{\text{fluid}}$	310 K
thermal conductivity	$k_{\text{thermal}}$	0.6 W/m/K
heat capacity	$C_p$	4200 J/kg/K
ratio of heat capacities	$\gamma$	1.02

Table 5: Viscous and thermal properties of the fluid around the robot, taken to be close to those of water and blood plasma [22, 35]. The heat capacity is at constant pressure and  $\gamma$  is the ratio of the value at constant pressure to that at constant volume.

as described in Appendix A. The first factor,  $\pi r_{\text{robot}}^2$ , is the geometric cross section of the robot. Since  $kr_{\text{robot}} \ll 1$ , the scattering cross section is much smaller than the robot’s size.

A hard sphere corresponds to  $\beta = 0$ , for which Eq. (15) becomes  $(4/9)\pi r_{\text{robot}}^2(kr_{\text{robot}})^4$  [27]. This is Rayleigh scattering, proportional to the fourth power of the sound’s frequency [57]. If the sphere’s center of mass is held in place rather than allowed to move in response to the sound, the cross section is a bit larger: the fraction is 7/9 instead of 4/9.

### 5.3 Viscous and Thermal Dissipation

Near the robot surface, viscous and thermal effects alter the sound propagation, which leads to dissipation. This occurs in viscous and thermal boundary layers with characteristic lengths  $\sqrt{2\eta/(\rho\omega)}$  and  $\sqrt{2k_{\text{thermal}}/(\rho C_p \omega)}$  for viscous and thermal dissipation, respectively [19, 20]. For the scenarios considered here, these boundary layers extend about a micron from the robot surface.

To evaluate these effects, we use viscous and thermal properties of water, given in Table 5. This is reasonable for robots in the bloodstream: because the boundary layers are small, the properties of blood determine behavior in the boundary layers around the robots, rather than the properties of the tissues through which the vessels are passing. This contrasts with using tissue attenuation properties for the sound propagation (see Table 1) since the wavelengths are large compared to size of most vessels.

The dissipation due to viscosity and thermal conduction in these boundary layers is proportional to  $(4/3)\eta + \eta_{\text{bulk}}$  and  $k_{\text{thermal}}(\gamma - 1)/C_p$ , respectively. With the parameters used here, these values are  $4 \times 10^{-3}$  Pa s and  $3 \times 10^{-6}$  Pa s, respectively. Thus, as is commonly the case for sound propagation in liquids, viscous dissipation is much larger than that due to thermal conduction.

Analytic models of sound scattering can include these boundary layers [20]. Alternatively, numerical evaluation of the dissipation readily incorporates the approximate uniform surface motion in response to the sound described above. This gives dissipation from both the tissue (see Table 1) and the boundary layers around the sphere. Numerically evaluating the pressure with viscous and thermal dissipation [19] for cases with and without the sphere allows determining the increased dissipation due to the presence of the robot. Without the sphere, dissipation arises only from tissue attenuation. The difference between these two cases gives the dissipation due to the viscous and thermal boundary layers. As expected for sound in liquids, viscous dissipation is much larger than that due to thermal effects. Dividing this dissipation by the flux of the incident plane wave gives the cross section for dissipation in the fluid around the sphere.

Viscous losses in the boundary layer around an object arise from no-slip condition at its surface. Appropriately designed surfaces could reduce this dissipation, as discussed in Section 3.2.1. In addition, the robot surface may be built to allow tangential motion, e.g., because combinations of both radial and tangential motion can improve the efficiency of locomotion based on surface vibrations [30]. A surface with some tangential motion, along with the radial piston motion, could more closely match the acoustic motion of fluid when there is no robot. Such a surface will have less effect on the sound wave than a tangentially rigid surface, and hence less viscous dissipation.

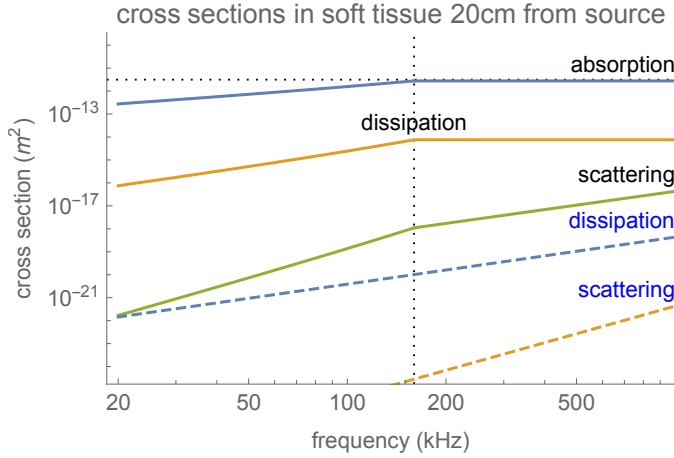


Figure 7: Cross sections vs. frequency for a single robot, with 20 pistons, located in soft tissue 20 cm from a 50 kPa transducer. The curves show cross sections for energy absorbed by the pistons, dissipation in the fluid around the robot and energy scattered by the robot. For comparison, the dashed curves show cross sections for dissipation and scattering by a hard sphere, corresponding to a robot with pistons locked at their limit of motion so they don't respond to the acoustic pressure. The dotted horizontal line is the geometric cross section of the robot,  $\pi r_{\text{robot}}^2$ . The vertical dotted line is the frequency, 160 kHz, at which  $\lambda = 2$  (see Eq. (9)).

number	typical spacing	number density
$10^{10}$	$170 \mu\text{m}$	$2 \times 10^{11}/\text{m}^3$
$10^{11}$	$80 \mu\text{m}$	$2 \times 10^{12}/\text{m}^3$
$10^{12}$	$40 \mu\text{m}$	$2 \times 10^{13}/\text{m}^3$

Table 6: Scenarios with various numbers of robots in a body with volume  $V_{\text{body}} = 50 \text{ L}$ . The typical spacing is the average distance between neighboring robots, estimated as the cube root of the average volume per robot.

#### 5.4 Attenuation Cross Sections for a Robot

Fig. 7 shows the contributions of processes removing energy from a plane wave for a robot in soft tissue 20 cm from the ultrasound source, the same scenario as in Fig. 6. The total cross section for removing energy from the sound wave is the sum of these three contributions. As illustrated in this figure, absorption is the dominant contribution, i.e., the pistons extract significantly more energy from the sound than dissipation in boundary layers, which in turn is much larger than the scattered energy. The figure also shows cross sections for a hard sphere, corresponding to locked pistons when the robot is not collecting energy. These are much less than when robots absorb power.

#### 5.5 Sound Attenuation by a Swarm of Robots

Prior studies of powering microscopic robots focus on one or a few nearby robots [22, 32]. This is adequate to evaluate the power available to individual robots and how power distributes among nearby robots. In the case of acoustic power, Fig. 7 shows the cross sections for a single robot are very small. Thus, a few microscopic robots will not significantly alter the intensity of sound with wavelengths substantially larger than the robots. This means that the power available to a robot is not affected by a few other robots at distances large compared to the robot's size.

However, proposed applications involve large numbers of robots [22]. These robots not only compete for power directly with nearby robots, but also deplete the power source globally. This is a particular concern for acoustics, where the power source is outside the body: robots in the

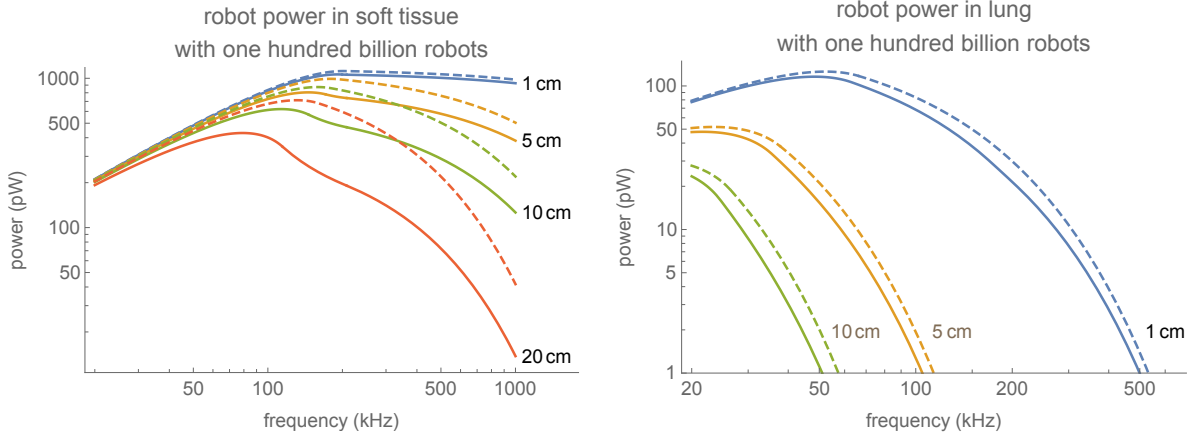


Figure 8: Power with attenuation due to  $10^{11}$  uniformly-distributed robots collecting power (solid curves) for the scenario of Table 4. The dashed curves show power without robot attenuation, from Fig. 6.

body could significantly attenuate sound reaching deep into the body, analogous to the increased attenuation due to bubbles [1].

Thus accessing the applicability of acoustic power to swarms of microscopic robots requires estimating how large numbers affect sound propagation. To do so, this section applies the effect of a single robot, described in Section 5.4, to evaluate attenuation due to many robots for the scenarios in Table 6.

Assuming robots are randomly positioned in the body, scattering from the robots is incoherent. Thus attenuation from a group of robots is the sum of that from each robot individually. In this case, robots with number density  $\nu_{\text{robot}}$  and cross section  $\sigma$  give amplitude attenuation

$$\alpha_{\text{robot}} = \frac{1}{2} \nu_{\text{robot}} \sigma \quad (16)$$

The attenuation for power is twice this value.

For robots uniformly distributed throughout the body  $\nu_{\text{robot}}$  is the ratio of number of robots to the body volume. There could be some variation in this value. E.g., if robots are uniformly distributed in the blood volume, then parts of the body with high or low blood supply will have correspondingly higher or lower  $\nu_{\text{robot}}$ . If, instead, robots concentrate in a portion of the body, e.g., a single organ, the corresponding number density for a given number of robots will be larger in that region, with correspondingly larger attenuation, and smaller elsewhere.

Fig. 7 shows that energy absorbed by the pistons is the dominant contribution to a robot's acoustic cross section. Thus we use power absorption to evaluate the effect of large numbers of robots. As an example, Fig. 8 shows how  $10^{11}$  robots affect power at various distances from the source. Comparing with Fig. 6 shows the robots significantly reduce power in soft tissue at the higher frequencies and distances. On the other hand, attenuation in lung is so large that robots add a relatively minor amount to the attenuation. Attenuation in soft tissue increases rapidly with additional robots, as shown in Fig. 9.

For the scenario of Fig. 8, averaging over locations in the body,  $10^{11}$  robots could each collect around 100 pW, so the total power collected by all the robots is tens of watts. In this example, transducers deliver  $1000 \text{ W/m}^2$  over much of the body's surface, so the total power is about 1000 W. Thus robots extract only a small portion of the delivered acoustic power.

Robot power extraction depends on pressure (see Section 3.4). Hence the robots' contribution to attenuation is pressure-dependent. At low frequencies and small distances, pressure is large, so the piston range limits the amount of energy robots can extract from the acoustic wave. In that case,

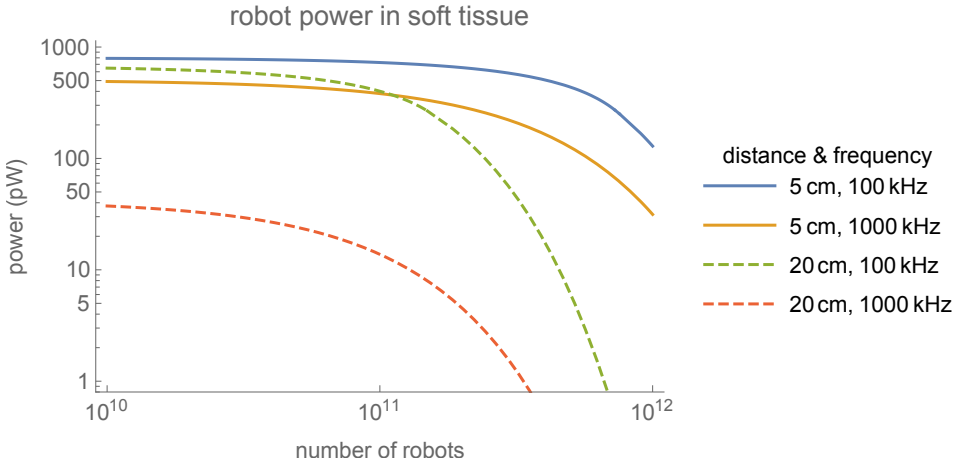


Figure 9: Power with attenuation due to robots collecting power in soft tissue as a function of number of robots uniformly distributed in the body volume for the scenario of Table 4. The curves correspond to the indicated distances from the source and sound frequencies.

robots add relatively little to the attenuation. However, when pressure decreases enough so that pistons do not move through their full range of motion, robots extract significant power and greatly increase the attenuation. Since pressure decreases with distance from the transducers, robot-induced attenuation is particularly large far from the transducers, i.e., where power is already relatively low due to tissue attenuation.

## 6 Compensating for Swarm Attenuation

Section 5.5 shows that a swarm of microscopic robots significantly increases attenuation in tissue. Unlike passive particles, microscopic robots can coordinate their behavior [29] to mitigate this problem by altering the distribution of sound in both time and space to flexibly allocate power among robots in the swarm. This section describes several mitigation strategies robots could use individually or in combination, possibly at different times or locations. This swarm behavior can be particularly beneficial for robot missions with temporally distinct phases requiring different amounts of power in different locations depending on each robot’s local environment.

### 6.1 Adjusting Mission Scope and Timing

A direct way to avoid significant attenuation is selecting tasks for the robots that do not require large numbers, e.g., using well below  $10^{12}$  in soft tissue (see Fig. 9). However, this may limit the speed or effectiveness of applications, particularly those requiring significant concentrations of robots acting at the same time, such as collecting data simultaneously from many cells, comparing observations with those of neighboring robots, or requiring many robots to act simultaneously on many cells.

Another strategy to cope with low power far from the source is for robots to adjust their activities based on available power. For example, robots have more power when they are near the skin than when deep in tissue. Thus a robot could defer power-intensive tasks, such as data analysis or communication, until they are near the skin. Conversely, robots deeper in tissue could perform only the most immediately relevant tasks, or only operate intermittently.

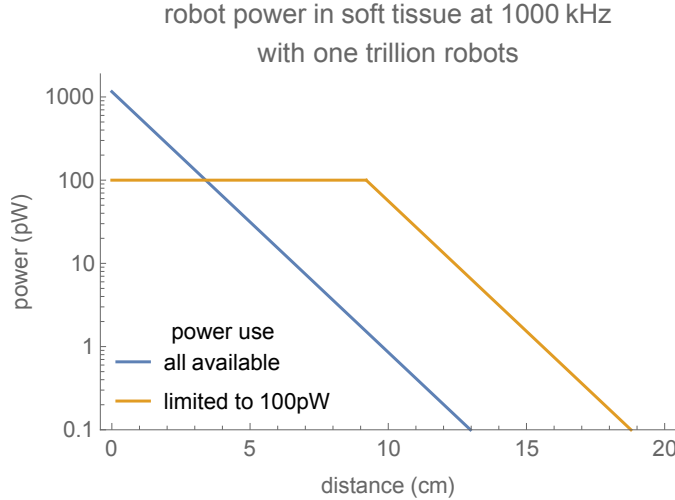


Figure 10: Power with  $10^{12}$  robots for sound with 1000 kHz for the scenario of Table 4. The curves show power when robots use all available power and when they each use at most 100 pW.

## 6.2 Storing Energy

This study evaluates the steady-state power available from acoustic pressure. Instead of using the power as received, a robot could store energy for later use [22]. Stored energy can provide higher burst power, or power when the robot is in a location where the sound is too attenuated to provide adequate power. Energy storage allows separating when energy is collected from when it is used. A limitation of this approach is that storage mechanisms could require a significant fraction of the robot volume.

Robots that move through the body continually change their distances from the skin. If robots have sufficient energy storage, they could collect enough power when near the skin to power their activities deeper in the body, or when they pass into high-attenuation tissues, such as lung. An example is robots delivering oxygen [21] to supplement that from red blood cells. The main activity of such robots is pumping oxygen and carbon dioxide into or out of tanks. This occurs while they are in capillaries, which is only a few percent of the time they circulate in the blood [22]. These robots would have little acoustic power while in the lung, so would need to collect energy prior to entering the lung.

Energy storage could also be useful when using a mix of robot sizes. That is, larger robots, stationed at fixed locations rather than being small enough to travel through capillaries, could collect and store energy. By vibrating their surfaces, such robots could act as small transducers distributed within the tissue, providing power to smaller robots as they pass nearby. This power transmission would occur over much smaller distances than power from external transducers, so could use higher frequencies that would significantly attenuate if used by the external transducers. These larger robots could exploit the acoustic efficiency of higher frequencies [33] to provide both power and communication, while receiving power over longer distances by using lower frequencies.

## 6.3 Limiting Robot Power Collection

Acoustic attenuation produces a highly nonuniform distribution of power in the body. Robots absorbing power increase attenuation and thus increase this variation. This means robots near the skin have a great deal of power, while those deeper in the body have little.

Robots near the skin could reduce this power gradient by limiting their power collection, e.g., by locking some pistons in place. Alternatively, a robot could reduce the power collected by each piston. This could involve slower motion (by increasing the load on each piston) or stopping pistons

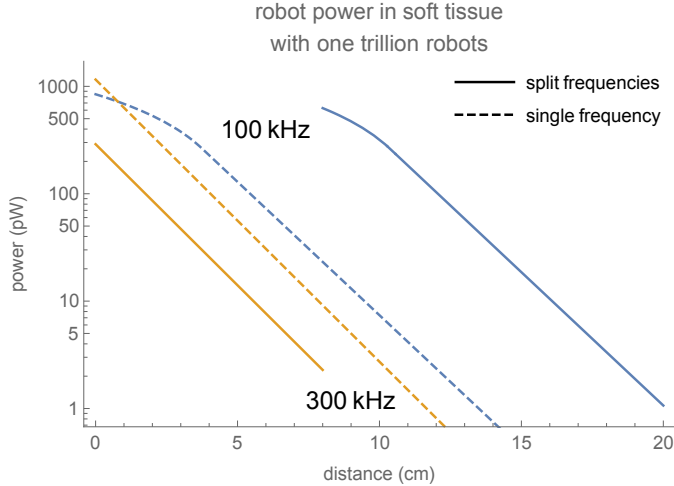


Figure 11: Power with  $10^{12}$  robots. The solid curves show power for the scenario of Table 4, except the  $1000 \text{ W/m}^2$  source intensity is split between 100 kHz and 300 kHz, with source pressures 43 kPa and 23 kPa, respectively. Robots use the higher frequency at small depths and the lower frequency at large depths. The dashed curves show power available when all robots extract power from just one of the frequencies, each with source intensity of  $1000 \text{ W/m}^2$ .

during a portion of each acoustic cycle (e.g., by reducing the range of piston motion). For the same power, the latter approach leads to more dissipation, and hence higher attenuation. Thus slowing piston speed is the better option.

Stopping piston motion over several acoustic cycles rather than just part of one has an additional benefit if robots near the skin synchronize their duty cycles for absorbing power: while all robots near the skin stop absorbing power, they reduce sound attenuation, making bursts of higher power available to deeper tissue. This contrasts with unsynchronized duty cycles, which only somewhat increases average power to deeper robots. A synchronization signal could be added to the sound wave from transducers, or could be provided from clocks in the robots.

Another option is to select the range of pistons so that high pressure variation pushes them to their limits. While stuck at their limits, pistons do not absorb power. In this case, robots less than half a wavelength apart would automatically be approximately synchronized by experiencing extreme pressure variations at about the same time. This is particularly useful for robots intended to operate near the skin. Such robots can get significant power without a large range for pistons and will have more of their volume available for other uses.

Collecting less power reduces the major contribution to acoustic attenuation even though these robots still attenuate sound through dissipation in the boundary layer and by scattering (see Fig. 7). As an example of this strategy, Fig. 10 shows a situation with such a large number of robots that little power remains 20 cm from the source (see Fig. 9). In this case, robots that limit their power considerably increase the depth at which other robots receive substantial power.

## 6.4 Using Multiple Frequencies

Using two or more frequencies can provide more power to robots deeper in the body. With this approach, robots near the skin extract power from a higher frequency, while a lower frequency, with lower attenuation, is reserved for deeper robots. By not extracting power from the low frequency, these robots only passively attenuate the sound, i.e., by scattering and viscous dissipation in fluid around the robot. This passive attenuation is significantly less than attenuation due to power extraction (see Fig. 7).

A limitation of this approach is that the combined intensity of the frequencies must not exceed

the safe limit on total intensity. Thus splitting the sound among two or more frequencies means less power from each frequency than if using that frequency alone.

Fig. 11 is an example of this strategy. Robots monitor the power available from the higher frequency, and use that frequency for power when it provides at least 2.3 pW, which occurs at a distance of 8 cm from the source. Otherwise they switch to the lower frequency. In this case, robots 10 cm from the source have more power than those a bit closer to the skin, so acoustic power is not a monotonic function of distance into the body. This split-frequency approach provides significantly more power to deeper robots than when all robots use just one of these frequencies.

To apply this technique, robots near the skin adjust their springs to avoid responding to the low frequency, in the same way they compensate for variations in ambient pressure, as discussed with Eq. (8). As an example, adjusting the constant-force spring to compensate for 100 kHz pressure variation requires changing the overlap,  $L_{\text{spring}}$ , much more rapidly than needed to adjust for changes in ambient pressure. As an extreme case, consider a robot close to a source with 50 kPa pressure amplitude. It must adjust for pressure changing by twice this amount each half-period of the acoustic wave. This corresponds to changing  $L_{\text{spring}}$  by about 35 nm in 5  $\mu$ s. From Eq. (6) and using the upper bound on  $L_{\text{spring}}h_{\text{spring}}$  of  $0.01 \mu\text{m}^2$ , this adjustment dissipates less than  $10^{-3}$  pW. While far larger than the power dissipated to adjust to ambient pressure variation (see Section 3.2.1), this dissipation is much less than the power available to the robot.

In some applications, robots may remain in one location for an extended period of time, e.g., to collect measurements on individual cells throughout the cell cycle. This task could benefit from different classes of robots. E.g., robots designed to work in high-power environments near the skin could only use high frequencies and hence could have fewer, shallower pistons, since their range of motion is less at high frequencies. Such pistons would not be as effective at collecting power from lower frequencies. On the other hand, robots intended for deeper operation could devote more of their volume to pistons to more efficiently collect power from lower frequencies. This, a heterogeneous mixture of robots could better match the availability of acoustic power than if all robots have the same design. Moreover, evolutionary algorithms can adapt the fraction of different types in such heterogeneous swarms [39].

## 6.5 Positioning Robots to Provide Low-Attenuation Paths

Robots avoiding locations between skin and a region of deeper tissue can allow more sound to reach robots in that deeper region. These regions may not be static, e.g., some tissue moves a few centimeters during each breath, which is larger than the wavelengths considered here. Robots must adjust for this motion if it changes their positions relative to the deeper locations that require the additional power. They could do so either locally, by comparing positions relative to nearby robots, or via external signals from imaging, such as used with radiological treatments [42].

If deeper robots do not require continuous power, robots could employ this mitigation only as needed, thereby alternating power between deeper and shallower robots. This could occur on a periodic schedule to provide a predictable duty cycle of power to the deeper robots. Alternatively, the occasional power needs of deeper robots could occur in response to events in their local environment, such as when sensing specific patterns of chemicals that require significant computational analysis or communication to other robots. In such cases, the robots could communicate their need for additional power, either directly or via neighbors, to shallower robots, requesting that those robots cease their power use to allow more power to reach the deeper robot. This approach to occasional power is an alternative to robots collecting and storing energy for occasional burst use (see Section 6.2). Creating low-attenuation paths to deeper tissue is particularly attractive when onboard energy storage would require too much of the robot volume to support the required burst power.

With this method of sharing acoustic power, robots manage energy collection and use as a group, rather than each robot focusing only on its own energy requirements. This approach is especially useful if the main power-using activities are in relatively small deep regions of the body.

Fig. 12 is an example of this strategy where robots avoid paths between transducers on the

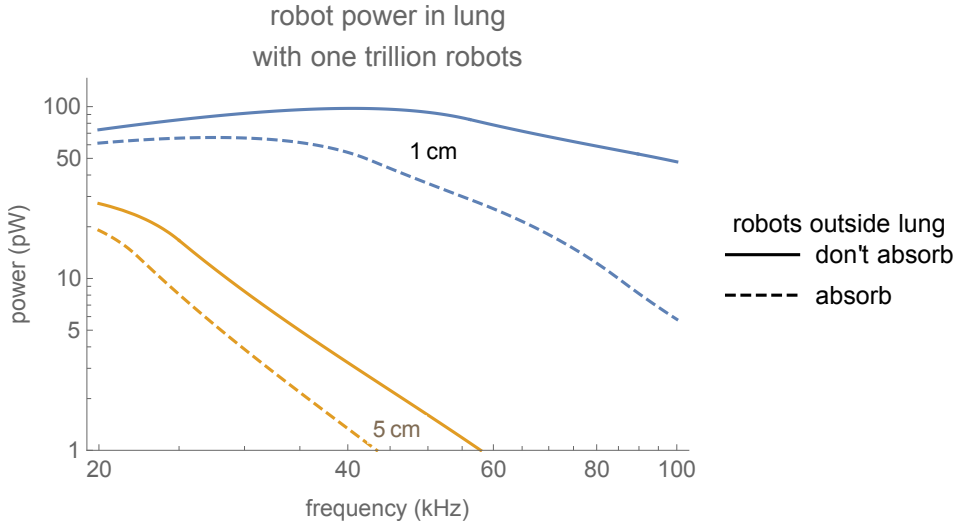


Figure 12: Power for robots in the lung with  $10^{12}$  robots in the body for the scenario of Table 4. The solid curves show power when robots avoid locations between the lung surface and the skin. For comparison, the dashed curves show power when uniformly distributed robots absorb power at all locations, including between the lung and the skin. The values next to the curves indicate distance from the skin-facing surface of the lung.

skin and the surface of the lung. In this case, the number of robots is large enough to considerably attenuate the sound in the tissue between the lung and the skin (see Fig. 9). Avoiding those locations provides more power to robots in the lung.

Ideally, for this strategy, the robots would actively avoid the path regions. Thus they would not contribute to attenuation by any of the mechanisms in Fig. 7. However, moving robots out of some regions leads to higher concentrations in others, thereby increasing attenuation in those regions above the values described in Section 5.5 for a uniform distribution of robots.

Even if robots cannot control their movements, they could achieve much of the same effect by stopping or reducing their power absorption when they detect they are passing through path locations, e.g., indicated by navigation signals [22]. Identifying these locations would only need resolution comparable to a wavelength or larger, i.e., millimeters. Such robots would still attenuate sound due to scattering and dissipation near their surfaces, but much less than when they absorb power (see Fig. 7).

Shaping acoustic waves in desired configurations is an application of methods to design swarm behaviors that form specific global shapes [62, 71]. Combining these control design techniques with how robots affect acoustic waves, as discussed in Section 5.5, could allow a swarm to adjust available power in ways suited for specific robot missions. For example, robots able to move independently and measure their distances to neighbors could position themselves to precisely tune acoustic properties at scales well below the wavelength, thereby creating dynamic acoustic metamaterials [8, 38, 72]. In these materials, sound scatters coherently from the robots, in contrast to incoherent scattering used to evaluate the effect of many robots (see Eq. (16)). An application of such materials is focusing sound into small, deeper regions where some of the robots require additional power. Metamaterials can respond selectively to specific frequencies. This capability could enhance power distribution when robots use multiple frequencies, as described in Section 6.4. Specifically, the positioning of the swarm could direct the lower frequency toward robots that are deeper in the tissue to deliver power more precisely.

## 7 Conclusion

This paper evaluated ultrasonic power for swarms of microscopic robots using mechanical energy harvesters. Frequencies around 100 kHz provide the most power in much of the body. But robots more than a centimeter or so in high-attenuation tissue receive little power. Robots in such locations require other power sources [22], or they must store enough energy to support their operation. Even within a tissue with low attenuation, power can vary with small-scale changes in robot location. This is because power decreases with increasing viscosity of the fluid around the robot (see Eq. (13)). The scenarios of this paper correspond to robots in blood vessels. Robots outside of blood vessels could encounter much larger viscosities [22], and hence have less power than nearby robots in vessels.

Using more than about a hundred billion robots can significantly reduce power for robots far from the skin. This reduction would not be apparent in tests involving a small number of robots. Thus a method to power implanted devices that is adequate for a few robots could fail when applied to large numbers. In such situations, designing missions for microscopic robots could not consider robots independently even when the robots do not need to coordinate their behaviors to perform their tasks. Section 6 described some approaches to mitigate this effect.

Providing acoustic power to microscopic robots throughout the body requires continually operating transducers over a substantial fraction of the body surface so all robots are within a relatively short distance of a transducer. This raises two challenges.

First, treatments using transducers over much of the body would only occur in clinical settings. This is not suitable for long-term applications such as ongoing health monitoring. Instead, such acoustic power for long-term use would be delivered by only one or a few small transducers a person could continually wear. The power of such transducers would be limited by battery storage, and only provide significant power to small regions of the body near those transducers.

A second challenge arises from the total power applied by the transducers. While  $1000 \text{ W/m}^2$  is safely used routinely for imaging over a small area of the body [22], such transducers covering a significant fraction of the body surface, would deliver about 1000 W. This compares with the body's basal power use of about 100 W. For applications lasting a significant time, e.g., hours, this level of heating could require active cooling. If this is not feasible, long-lasting applications would require reducing sound intensity, thereby reducing the power available to the robots. Such reduction could be continuous, or occur through pauses in operation. These pauses could be brief, e.g., a duty cycle that powers the transducers one millisecond out of every 10. Such pauses would be tolerable if robots can store enough power to continue operation between acoustic bursts, or can accomplish their tasks with intermittent operation, e.g., for diagnostics that only need to sample the robot's environment after it moves to a new location.

Acoustic power poses challenges for robot design. While pistons are relatively simple energy collectors, they are also bulky, using a significant fraction of robot volume and surface, compared, for example, to chemical power from fuel cells [22,32]. Thus using enough pistons to collect adequate power may reduce performance of other uses of the robot volume or surface.

For example, a robot may require substantial volume for tanks of chemicals, energy storage or information processing. The robot could require surface area for a variety of tasks. One important task is surface devoted to chemical sensors or pumps. Such devices can be much smaller than the total surface area, allowing room for a large number of them [22]. For this task, pistons are not likely to be a major issue because chemical collection is only weakly dependent on the fraction of surface area absorbing the chemical [6]. However, area devoted to pistons could be more limiting for other uses. For example, communication [33] or locomotion [30] can require substantial surface area. A possible mitigation to these competing uses is for the pistons to perform multiple functions. For example, the actuators adjusting the spring's force in response to changing ambient pressure could also provide force to move the pistons. This could readily provide surface oscillations for locomotion, which involve lower frequencies (1–10 kHz) but similar range of motion [30] as the pistons considered here. Frequencies comparable to those used to receive power may be useful for robots to selectively destroy some types of diseased cells next to the robot [49]. On the other hand, actuating the pistons

for acoustic communication requires much higher frequencies and smaller ranges of motion [33], which may be beyond the capabilities of actuators involved in power collection by adjusting the springs in response to ambient pressure changes.

In light of these limitations, both for the patient and robot design, the relative simplicity of acoustic power is best suited to applications where robots perform relatively limited tasks that don't require lengthy on-going operation or many additional mechanisms inside, or on the surface of, the robot. These situations are particularly relevant for early applications of microscopic robots. More broadly, these considerations of the feasibility and challenges of acoustic power show that the choice of how to power microscopic robots strongly depends on the nature of their intended application and the number of robots used.

The results of this paper, as well as these future extensions, can identify applications of swarms of microscopic robots where acoustic power is a good option, as opposed to, for example, as magnetic fields or chemical power. Since power is a key requirement for these devices, this can inform the design of such robots when they become feasible to manufacture in large numbers.

This study highlights two broad directions for future study. The first is designing and building acoustic energy harvesters that best exploit the limited robot volume and surface area. Reducing the space required for powering the robot will leave more room for other components, thereby extending the range of missions robots can perform. One such improvement is developing nanoscale engineered surfaces with low viscous drag, as discussed in Section 3.2.1.

The second direction is evaluating available power in the complex acoustic environment of the body, including the effect of heterogeneous tissues, with widely varying acoustic properties, between the skin and the robots [67]. For example, the acoustic analysis described here focuses on longitudinal compression waves. This is reasonable for evaluating the sound absorbed by robots in the bloodstream. In general, propagation could be affected by other properties of biological tissues. In particular solid structures such as bone can also support shear waves, and wave propagation can vary with direction, i.e., forming nonisotropic elastic solids instead of simple fluids. These material properties could distribute acoustic energy differently than would be the case for purely longitudinal waves. Robot mission designs will need to account for these variations, which depend on both a robot's macroscale position in the body and the robot's immediate environment, e.g., within tens of microns. Available power will also depend on the locations and activities of other robots, both nearby and between the robot and the acoustic sources on the skin. Thus it will be important to evaluate how the mitigating strategies described in this paper perform with the variation in tissue properties and how swarms can adapt to those variations. Such studies could improve the ability of each robot to extract acoustic power and characterize how available power varies with location within the body.

## Acknowledgements

I have benefited from discussions with Robert Freitas Jr., Ralph Merkle, Matthew Moses and James Ryley.

## A Appendix: Scattering Cross Section

We evaluate the sound scattered by a sphere of radius  $a$  in response to an incident plane wave using the boundary conditions described in Section 5.1: the radial velocity of the sphere's surface equals the sum of  $-\beta p_{\text{inc}}(t)$  and the radial component of the periodic fluid velocity induced by the plane wave on the sphere's center of mass. For evaluating scattering, we neglect dissipative effects, which are treated separately in Section 5.3.

For this discussion, we express pressure and velocity in terms of complex-valued amplitudes  $p$  and  $v$ , respectively, and time-dependence  $e^{-i\omega t}$  where  $\omega = 2\pi f$  is the angular frequency. The actual values are the real parts, e.g., the pressure is  $\Re(pe^{-i\omega t})$ , where  $\Re$  denotes the real part. For acoustic

waves, pressure and velocity amplitudes are related by [19]

$$v = -\frac{i}{\omega\rho} \nabla p \quad (17)$$

and the amplitudes satisfy the Helmholtz equation

$$\nabla^2 p + k^2 p = 0 \quad (18)$$

where  $k = \omega/c$  is the wave number. The time-average flux is

$$\mathcal{F} = \frac{1}{2} \Re(vp^*) \quad (19)$$

where  $p^*$  is the complex-conjugate of  $p$  [19].

A convenient representation for matching boundary conditions on a sphere is expressing the pressure in spherical coordinates centered on the sphere with the  $z$  direction chosen to be the direction of the incident plane wave's motion. The total sound pressure is the sum of incident and scattered waves:  $p = p_{\text{inc}} + p_s$ .

The pressure amplitude of the incident plane wave propagating along the  $z$ -axis is  $p_{\text{inc}} = p_0 e^{ikz}$  where  $p_0$  is the pressure magnitude of the wave. In spherical coordinates,  $z = r \cos(\theta)$  so expressing the plane wave in solutions to the wave equation in spherical coordinates gives the pressure as a sum over modes [19, 64]:

$$p_{\text{inc}} = p_0 \sum_{m=0}^{\infty} F_m P_m(\cos \theta) j_m(kr) \quad (20)$$

where  $F_m = i^m (2m+1)$ ,  $P_m$  is the Legendre polynomial of order  $m$ , and  $j_m$  is the spherical Bessel function of order  $m$ . From Eq. (17), the corresponding velocity amplitude, in the  $z$  direction, is  $v_{\text{inc}} = p_0/(\rho c) e^{ikz}$ . The radial component of this velocity is  $v_{\text{inc}} \cos(\theta)$ .

Similarly, the amplitude of the scattered pressure,  $p_s$ , is an outgoing wave with expansion [19]

$$p_s = p_0 \sum_{m=0}^{\infty} A_m P_m(\cos \theta) h_m^{(1)}(kr) \quad (21)$$

where  $h_m^{(1)}$  is the spherical Hankel function of the first kind of order  $m$ , and the coefficients  $A_m$  are determined by matching the boundary condition at the surface of the sphere, as described below.

At the surface of the sphere, the radial component of the sound's velocity amplitude matches the specified boundary condition. From Eq. (17), this condition is

$$-\frac{i}{\omega\rho} \frac{\partial p}{\partial r} = -\beta p_{\text{inc}} + v_{\text{inc}} \cos(\theta) \quad (22)$$

evaluated at  $r = a$ , the radius of the sphere and  $v_{\text{inc}}$  evaluated at the sphere's center of mass, i.e.,  $z = 0$ . Substituting the above expansions for the incident and scattered waves in this equation gives a relation that must hold for all polar angles  $\theta$ . This requires matching each mode separately, thereby determining the coefficients  $A_m$  of the scattered wave. In particular, since  $P_1(x) = x$ , the incident velocity  $v_{\text{inc}}$  only contributes to mode  $m = 1$ .

The time-average flux of the incident plane wave,  $\mathcal{F}_{\text{inc}}$ , from Eq. (19) equals Eq. (14) with  $p$  replaced by  $p_0$ . Eq. (19) gives the scattered flux,  $\mathcal{F}_s$ , in terms of the coefficients  $A_m$ . For a spherical surface  $S$  of radius  $r$  centered on the scattering sphere, the total scattered power is the integral of  $\mathcal{F}_s$  over the surface  $S$ . Thus the scattering cross section is

$$\sigma = \frac{1}{\mathcal{F}_{\text{inc}}} \int_S \mathcal{F}_s dS \quad (23)$$

where  $dS = r^2 \sin(\theta) d\theta d\phi$  is the differential surface area for the sphere, with polar and azimuthal angles,  $\theta$  and  $\phi$ , respectively. The scattered sound spreads over the sphere but is not attenuated in this model. Thus the integral is independent of radius  $r$ .

When the sound wavelength is large compared to the sphere's radius, i.e.,  $ka \ll 1$ , only modes  $m = 0$  and  $m = 1$  contribute significantly to the scattered sound. This long-wavelength limit applies to the scenarios considered here (see Table 2). In this case, the coefficients are

$$\begin{aligned} A_0 &= \frac{2}{3}\beta c\rho(ka)^4 - \frac{1}{3}i(ka)^3 - \beta c\rho(ka)^2 \\ A_1 &= -\frac{1}{2}i\beta c\rho(ka)^4 \end{aligned} \quad (24)$$

Using these values in Eq. (23) gives the scattering cross section of Eq. (15) for the sphere with radius  $a = r_{\text{robot}}$ .

## References

- [1] Michael A. Ainslie and Timothy G. Leighton. Review of scattering and extinction cross-sections, damping factors, and resonance frequencies of a spherical gas bubble. *J. of the Acoustical Society of America*, 130:3184–3208, 2011.
- [2] Hamed Alemanpour et al. Controlled removal of hydrogen atoms from h-terminated silicon surfaces. *J. of Vacuum Science & Technology B*, 38:040601, 2020.
- [3] Achraf Ben Amar, Ammar B. Kouki, and Hung Cao. Power approaches for implantable medical devices. *Sensors*, 15:28889–28914, 2015.
- [4] Gaurav Arya, Hsueh-Chia Chang, and Edward J. Maginn. Molecular simulations of Knudsen wall-slip: Effect of wall morphology. *Molecular Simulation*, 29:697–709, 2003.
- [5] Kateryna Bazaka and Mohan V. Jacob. Implantable devices: Issues and challenges. *Electronics*, 2:1–34, 2013.
- [6] Howard C. Berg. *Random Walks in Biology*. Princeton Univ. Press, 2nd edition, 1993.
- [7] Allan M. Brooks and Michael S. Strano. A conceptual advance that gives microrobots legs. *Nature*, 584:530–531, 2020.
- [8] Huanyang Chen and C. T. Chan. Acoustic cloaking and transformation acoustics. *J. of Physics D: Applied Physics*, 43:113001, 2010.
- [9] K. A. Cook-Chennault, N. Thambi, and A. M. Sastry. Powering MEMS portable devices – a review of non-regenerative and regenerative power supply systems with special emphasis on piezoelectric energy harvesting systems. *Smart Materials and Structures*, 17:043001, 2008.
- [10] John Cumings and A. Zettl. Low-friction nanoscale linear bearing realized from multiwall carbon nanotubes. *Science*, 289:602–604, 2000.
- [11] Berta Esteban-Fernandez de Avila et al. Hybrid biomembrane-functionalized nanorobots for concurrent removal of pathogenic bacteria and toxins. *Science Robotics*, 3:eaat0485, 2018.
- [12] Alexey Denisov and Eric Yeatman. Stepwise microactuators powered by ultrasonic transfer. *Procedia Engineering*, 25:685–688, 2011.
- [13] Lixin Dong and Bradley J. Nelson. Robotics in the small. part II: Nanorobotics. *IEEE Robotics & Automation Magazine*, 14:111–121, 2007.
- [14] Shawn M. Douglas, Ido Bachelet, and George M. Church. A logic-gated nanorobot for targeted transport of molecular payloads. *Science*, 335:831–834, 2012.
- [15] M. R. Douglass. Lifetime estimates and unique failure mechanisms of the digital micromirror device (DMD). In *Proc. of the 1998 IEEE International Reliability Physics Symposium*. IEEE, 1998.

- [16] K. Eric Drexler. *Nanosystems: Molecular Machinery, Manufacturing, and Computation*. John Wiley, NY, 1992.
- [17] Fengzhou Fang et al. Towards atomic and close-to-atomic scale manufacturing. *Intl. J. of Extreme Manufacturing*, 1:012001, 2019.
- [18] James J. Faran Jr. Sound scattering by solid cylinders and spheres. *J. of the Acoustical Society of America*, 23:405–418, 1951.
- [19] Alexander L. Fetter and John Dirk Walecka. *Theoretical Mechanics of Particles and Continua*. McGraw-Hill, NY, 1980.
- [20] Peter Fleckenstein, Giuseppe Stortia, Fabian Deschwanden, Peter Gruber, and Marco Lattuada. Modeling analysis of ultrasonic attenuation and angular scattering measurements of suspended particles. *J. of the Acoustical Society of America*, 143:1049–1063, 2018.
- [21] Robert A. Freitas Jr. Exploratory design in medical nanotechnology: A mechanical artificial red cell. *Artificial Cells, Blood Substitutes and Immobilization Biotechnology*, 26:411–430, 1998.
- [22] Robert A. Freitas Jr. *Nanomedicine*, volume I: Basic Capabilities. Landes Bioscience, Georgetown, TX, 1999. Available at [www.nanomedicine.com/NMI.htm](http://www.nanomedicine.com/NMI.htm).
- [23] Robert A. Freitas Jr. and Ralph C. Merkle. *Kinematic Self-Replicating Machines*. Landes Bioscience, Georgetown, TX, 2004. Available at [www.MolecularAssembler.com/KSRM.htm](http://www.MolecularAssembler.com/KSRM.htm).
- [24] Steve Granick, Yingxi Zhu, and Hyunjung Lee. Slippery questions about complex fluids flowing past solids. *Nature Materials*, 2:221–227, 2003.
- [25] A. C. R. Grayson et al. A BioMEMS review: MEMS technology for physiologically integrated devices. *Proc. of the IEEE*, 92:6–21, 2004.
- [26] John Happel and Howard Brenner. *Low Reynolds Number Hydrodynamics*. Kluwer, The Hague, 2nd edition, 1983.
- [27] Sascha Hilgenfeldt and Detlef Lohse. Response of bubbles to diagnostic ultrasound: a unifying theoretical approach. *European Physics Journal B*, 4:247–255, 1998.
- [28] Ronan Hinchet et al. Transcutaneous ultrasound energy harvesting using capacitive triboelectric technology. *Science*, 365:491–494, 2019.
- [29] Tad Hogg. Coordinating microscopic robots in viscous fluids. *Autonomous Agents and Multi-Agent Systems*, 14(3):271–305, 2007.
- [30] Tad Hogg. Using surface-motions for locomotion of microscopic robots in viscous fluids. *J. of Micro-Bio Robotics*, 9:61–77, 2014.
- [31] Tad Hogg. Stress-based navigation for microscopic robots in viscous fluids. *J. of Micro-Bio Robotics*, 15:59–67, 2018.
- [32] Tad Hogg and Robert A. Freitas Jr. Chemical power for microscopic robots in capillaries. *Nanomedicine: Nanotechnology, Biology, and Medicine*, 6:298–317, 2010.
- [33] Tad Hogg and Robert A. Freitas Jr. Acoustic communication for medical nanorobots. *Nano Communication Networks*, 3:83–102, 2012.
- [34] Tad Hogg, Mathew S. Moses, and Damian G. Allis. Evaluating the friction of rotary joints in molecular machines. *Molecular Systems Design & Engineering*, 2:235–252, 2017.
- [35] M. J. Holmes, N. G. Parker, and M. J. W. Povey. Temperature dependence of bulk viscosity in water using acoustic spectroscopy. *J. of Physics: Conference Series*, 269:012011, 2011.

- [36] Stephen Hsu, Charles Ying, and Fei Zhao. The nature of friction: A critical assessment. *Friction*, 2:1–26, 2014.
- [37] Edwin W. H. Jager, Olle Inganas, and Ingemar Lundstrom. Microrobots for micrometer-size objects in aqueous media: Potential tools for single-cell manipulation. *Science*, 288:2335–2338, 2000.
- [38] Muamer Kadic, Tiemo Buckmann, Robert Schittny, and Martin Wegener. Metamaterials beyond electromagnetism. *Reports on Progress in Physics*, 76:126501, 2013.
- [39] Daniela Kengyel et al. Potential of heterogeneity in collective behaviors: A case study on heterogeneous swarms. In Q. Chen et al., editors, *Proc. of the Intl. Conf. on Principles and Practice of Multi-Agent Systems*, pages 201–217. Springer, 2015.
- [40] Chulki Kim, Robert Marsland, and Robert H. Blick. The nanomechanical bit. *Small*, 2020.
- [41] Elisa E. Konofagou. Trespassing the barrier of the brain with ultrasound. *Acoustics Today*, 13(4):21–26, Winter 2017.
- [42] S. S. Korreman. Image-guided radiotherapy and motion management in lung cancer. *The British Journal of Radiology*, 88:20150100, 2021.
- [43] Eric Lauga, Michael Brenner, and Howard Stone. Microfluidics: The no-slip boundary condition. In C. Tropea et al., editors, *Springer Handbook of Experimental Fluid Mechanics*, chapter 19, pages 1219–1240. Springer, 2007.
- [44] Jinxing Li, Berta Esteban-Fernandez de Avila, Wei Gao, Liangfang Zhang, and Joseph Wang. Micro/nanorobots for biomedicine: Delivery, surgery, sensing, and detoxification. *Science Robotics*, 2:eaam6431, 2017.
- [45] Ze Liu et al. Interlayer binding energy of graphite: A mesoscopic determination from deformation. *Physical Review B*, 85:205418, 2012.
- [46] Sylvain Martel et al. Flagellated bacterial nanorobots for medical interventions in the human body. In D. Meldrum and O. Khatib, editors, *Proc. of 2nd IEEE Conf. on Biomedical Robotics and Biomechatronics*, pages 264–269, 2008.
- [47] C. Mathew Mate. *Tribology on the Small Scale: A Bottom Up Approach to Friction, Lubrication, and Wear*. Oxford Univ. Press, 2008.
- [48] Ralph C. Merkle, Robert A. Freitas Jr., Tad Hogg, Thomas E. Moore, Matthew S. Moses, and James Ryley. Mechanical computing systems using only links and rotary joints. *ASME Journal on Mechanisms and Robotics*, 10:061006, 2018.
- [49] David R. Mittelstein et al. Selective ablation of cancer cells with low intensity pulsed ultrasound. *Applied Physics Letters*, 116:013701, 2020.
- [50] Sumit Mohanty, Islam S. M. Khalil, and Sarthak Misra. Contactless acoustic micro/nano manipulation: a paradigm for next generation applications in life sciences. *Proceedings of the Royal Society A: Mathematical, Physical and Engineering Sciences*, 476:20200621, 2020.
- [51] Kelly Morris. Macrodoctor, come meet the nanodoctors. *The Lancet*, 357:778, March 10 2001.
- [52] Bradley J. Nelson, Ioannis K. Kaliakatsos, and Jake J. Abbott. Microrobots for minimally invasive medicine. *Annual Review of Biomedical Engineering*, 12:55–85, 2010.
- [53] Kwan H. Ng. International guidelines and regulations for the safe use of diagnostic ultrasound in medicine. *J. of Medical Ultrasound*, 10:5–9, 2002.
- [54] Sumner L. Norman et al. Single-trial decoding of movement intentions using functional ultrasound neuroimaging. *Neuron*, 2021.

- [55] Aurea Pascal et al. Histologic evaluation of activation of acute inflammatory response in a mouse model following ultrasound-mediated blood-brain barrier using different acoustic pressures and microbubble doses. *Nanotheranostics*, 4:210–223, 2020.
- [56] Edward M. Purcell. Life at low Reynolds number. *American Journal of Physics*, 45:3–11, 1977.
- [57] Lord Rayleigh. The principle of similitude. *Nature*, 95:66–68, 1915.
- [58] S. W. Rienstra and A. Hirschberg. An introduction to acoustics. revised edition IWDE 92-06, Eindhoven Univ. of Technology, 2010.
- [59] Zaid Shaglwf, Bjorn Hammarstrom, Dina Shona Laila, Martyn Hill, and Peter Glynne-Jones. Acoustofluidic particle steering. *J. of the Acoustical Society of America*, 145:945–955, 2019.
- [60] H. Shankar and P. S. Pagel. Potential adverse ultrasound-related biological effects: a critical review. *Anesthesiology*, 115:1109–1124, 2011.
- [61] Q. Shi, T. Wang, and C. Lee. MEMS based broadband piezoelectric ultrasonic energy harvester (PUEH) for enabling self-powered implantable biomedical devices. *Scientific Reports*, 6:24946, 2016.
- [62] I. Slavkov et al. Morphogenesis in robot swarms. *Science Robotics*, 3:eaau9178, 2018.
- [63] Todd M. Squires and Stephen R. Quake. Microfluidics: Fluid physics at the nanoliter scale. *Reviews of Modern Physics*, 77:977–1026, 2005.
- [64] K. B. Sullivan-Silva. Underwater acoustic scattering from spherical particulates and bubbles. Technical Report 6772, NUSC, 1989.
- [65] S. N. Tabatabaei, H. Girouard, A. S. Carret, and S. Martel. Remote control of the permeability of the blood-brain barrier by magnetic heating of nanoparticles: A proof of concept for brain drug delivery. *J. Control Release*, 206:49–57, 2015.
- [66] Nimrod M. Tole. *Basic physics of ultrasonic imaging*. World Health Organization, 2005.
- [67] Bradley E. Treeby, Jari Jaros, Eleanor Martin, and Ben T. Cox. From biology to bytes: Predicting the path of ultrasound waves through the human body. *Acoustics Today*, 15(2):36–44, Summer 2019.
- [68] Emily Underwood. Can sound open the brain for therapies? *Science*, 347:1186–1187, 2015.
- [69] Xudong Wang et al. Direct-current nanogenerator driven by ultrasonic waves. *Science*, 316:102–105, 2007.
- [70] Michel Wautelet. Scaling laws in the macro-, micro- and nanoworlds. *European J. of Physics*, 22:601–611, 2001.
- [71] Justin Werfel, Kirstin Petersen, and Radhika Nagpal. Enzyme kinetics, past and present. *Science*, 343:754–758, 2014.
- [72] Nikolay L. Zheludev. The road ahead for metamaterials. *Science*, 328:582–583, 2010.
- [73] Marvin C. Ziskin. Fundamental physics of ultrasound and its propagation in tissue. *Radio-graphics*, 13:705–709, 1993.